Simulational and experimental investigation on the wavefront sensing method based on near-field profile acquisition in high power lasers

Deen Wang [a,b,c], Qiang Yuan [c], Ying Yang [c], Xin Zhang [c], Liangming Chen [c], Yamin Zheng [a,b], Dongxia Hu [c], Feng Jing [c], Qihua Zhu [c], Xiaofeng Wei [c], Wanguo Zheng [c], Xuewei Deng [c,*], Lei Huang [a,b,*]

[a] *Key Laboratory of Photonic Control Technology (Tsinghua University) Ministry of Education, Beijing, 10084, China*
[b] *State Key Laboratory of Precision Measurement Technology and Instruments, Department of Precision Instrument, Tsinghua University, Beijing 100084, China*
[c] *Research Center of Laser Fusion, CAEP, P.O. Box 919-988, Mianyang 621900, China*

ARTICLE INFO

ABSTRACT

This paper presents a novel wavefront sensing method based on near-field profile acquisition (NIA) to acquire the wavefront information. This method uses a cross mark at the focal plane of the spatial filter to directly obtain wavefront slope from the power spectral density (PSD) distribution of the output near-field profile. Principles of this method are introduced and the numerical simulation model is built. The influence of primary parameters on the measurement precision are analyzed and discussed. Based on the designed cross mark structure, an experiment is carried out in a multi-pass amplification high power laser and the wavefront of the pre-amplifier is reconstructed. Experimental results show that the difference between the reconstructed wavefronts by using the traditional Shack–Hartmann (SH) and the NIA wavefront sensing method is as small as 0.09 μm (peak-to-valley value).

1. Introduction

Wavefront distortion, resulted from imperfections and thermal effects of optical components, has become one of the major problems in the multi-pass amplification high power laser systems. It critically affects the clean transmission through the pinhole of the spatial filter, reduces energy coupling efficiency and degrades beam quality. In order to evaluate the wavefront distortion, various of wavefront sensing techniques with distinct characteristics have been proposed, including shearing or point-diffraction interferometry [1–3], holographic modal wavefront sensing [4–6], Shack–Hartmann (SH) wavefront sensing [7–9], curvature wavefront sensing [10–12], pyramid wavefront sensing [13,14] and some other new wavefront sensing methods such as extended Ptychographical Iterative Engine technique [15], surface-plasmon-based wavefront sensing [16], speckle-based phase retrieval method [17] and deep learning wavefront sensing [18], etc.

In the high power lasers for inertial confinement fusion (ICF) research, including the National Ignition Facility, the Laser MégaJoule Facility, the OMEGA extended performance Laser System and the Chinese ICF Facility, SH wavefront sensing has become the most widely used wavefront sensing approach for its adaptability and robustness [19–22]. Generally, when measuring wavefront using SH sensor, the wavefront of the diagnostic beamline should be calibrated firstly by the reference light without any distortions (i.e. the beam generated from a single mode fiber is inserted at the focal plan of the spatial filter). In practice, the fiber laser is an indispensable component for wavefront sensing in the high power laser [23], which causes time-consuming process and high cost, especially for the ICF laser facilities consisting hundreds of beamlines.

This paper presents a novel wavefront sensing method based on near-field profile acquisition (denoted as NIA wavefront sensing method). This method uses a cross mark (CM) at the focal plane of the optical route to directly obtain wavefront slope from the power spectral density (PSD) distribution of the output near-field profile. Compared to traditional wavefront sensing method, the presented NIA wavefront sensing method could conveniently acquire online wavefront without reference fiber light. This paper is organized as follows. In Section 2, the principles of the NIA wavefront sensing method is illustrated. Based on the principles, measurement process of the NIA wavefront sensing method is further proposed. In Section 3, a numerical simulation model is built and the influences of primary parameters on the measurement precision are analyzed and discussed. In Section 4, an experiment is carried out and the experimental results are discussed.
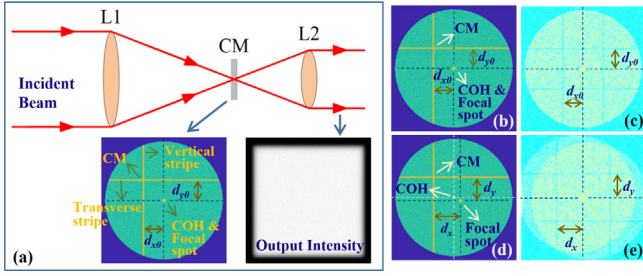

Fig. 1. Wavefront acquisition principle. (a) is the optical scheme. (b) is the logarithmic intensity of the ideal incident beam at the focal plane. (c) is the logarithmic PSD distribution of the output near-field profile of the ideal incident beam. (d) is the logarithmic intensity of the distorted incident beam at the focal plane. (e) is the logarithmic PSD distribution of the output near-field profile of the distorted incident beam.

2. Wavefront acquisition principle

In a spatial filter, as illustrated in Fig. 1(a), any modulation at the focal plane will convolve with the light field and influence the output near-field profile at the image plane, which could be detected by a charge coupled device (CCD) camera. According to the PSD definition based on convolution theorem, the relationship between the output intensity of the spatial filter and focal light field can be expressed in Eq. (1) [24].

$$\left| F\left\{ \left| \widetilde{E_1} \right|^2 \right\} \right|^2 = \left| \left(F\left\{ \widetilde{E_0} \right\} \cdot M \right) * \left(F\left\{ \widetilde{E_0} \right\} \cdot M \right) \right|^2. \tag{1}$$

where $\widetilde{E_0}$ is the incident light field, M is the transfer function, * the self-correlation operator, $\left| \widetilde{E_1} \right|^2$ the intensity of the light field at the imaging plane, M is the modulation function of the CM, and F{·} the Fourier transformation.

Fig. 1(a) shows a typical optical scheme, in which a hole with an off-centered cross mark (CM) is put at the focal plane. The CM comprises a vertical nontransparent stripe and a transverse nontransparent stripe, as shown in Fig. 1(a). Note that, the CM should be covered by the high spatial frequency components of the light field, so the incident beam is modulated by the high frequency amplitude noises in the simulation process, which is common in the actual laser system for fine material defects in optics. In general, the focal spot is several orders of magnitude (about 108 here) stronger than the high spatial frequency components dispersal around. In order to observe the information of the metal stripes at the focal plane and the PSD image, Fig. 1(b)–(e) are shown in logarithmic coordinates, and the information of the CM stripes are clear. If the wavefront of incident beam is ideal without any distortion, from the logarithmic intensity distribution displayed in Fig. 1(b), the focal spot locates right at the COH in the spectral plane. As the high spatial frequency components of the light field is modulated by the CM [Fig. 1(b)], according to Eq. (1), the stripes of the CM will bring four cross dark lines in the PSD distribution of the output nearfield profile [Fig. 1(c)], while the off-center distances of the dark lines are equal to the perpendicular distances (dx0, dy0) of the stripes from the COH respectively. If the incident beam is distorted, the focal spot will deviate from the COH at the focal plane [Fig. 1(d)]. From the PSD distribution calculated from the output near-field profile [Fig. 1(e)], the information of CM stripes and the circle hole will also shift due to the focal spot deviation according to Eq. (1) and the off-center distances of the four cross dark lines change are equal to the perpendicular distances (dx, dy) between the focal spot and the CM stripes. The variations of the off-center distances of the four cross dark lines represent the distances between the focal spots of the distorted beam and the ideal beam. Thus, the wavefront slopes of the distorted beam can be obtained by simply calculating the variation of the off-center distances of the four cross
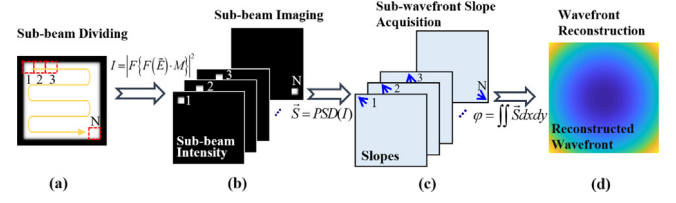
dark lines in the PSD distribution of the output near-field profile, as shown in Eq. (2).

$$S_x = \left(\overrightarrow{d_x} - \overrightarrow{d_{x0}} \right) / f, \quad S_y = \left(\overrightarrow{d_y} - \overrightarrow{d_{y0}} \right) / f. \tag{2}$$

where, S_x and S_y are the wavefront slopes in X-direction and Y-direction respectively and f is the focal length of the input lens of spatial filter [i.e. L1 in Fig. 1(a)].

Fig. 2 illustrates the wavefront measurement process of the NIA wavefront sensing method, which consists of four steps: the sub-beam dividing, sub-beam imaging, sub-wavefront slope acquisition and wave-front reconstruction. In the sub-beam dividing step [Fig. 2(a)], the incident beam is divided by a beam modulator (e.g. the liquid crystal on silicon modulator), which is always employed for the laser beam shaping [25,26]. By controlling the transmissivity of different segments in the beam modulator, the incident beam is divided into series of sub-beams. Each sub-beam enters into the spatial filter [Fig. 1(a)] and is modulated by the CM with the modulation function M [Eq. (1)]. After passing through the spatial filter [Fig. 1(a)], these sub-beams are detected by a CCD camera one by one [Fig. 2(b)]. Note that the interval time between two sub-beams are controlled by the beam modulator. In the sub-wavefront slope acquisition step [Fig. 2(c)], the PSD distribution of each sub-beam is calculated and the corresponding sub-wavefront slope is extracted. After acquiring all the sub-wavefront slopes from the sub-beams, a slope matrix is generated. Finally, the wavefront of the whole incident beam could be reconstructed from the slope matrix by means of a wavefront reconstruction algorithm [Fig. 2(d)].

Fig. 2. Wavefront measurement process of the NIA wavefront sensing method.

3. Simulation and analysis

As discussed above, by introducing the CM at the spectral plane and slightly modulating the high spatial frequency components of the light field, wavefront sensing could be achieved by directly acquiring the wavefront slope. According to Eqs. (1)–(2), the wavefront measurement accuracy is determined by the primary parameters of the CM, including the width of the CM stripe (WMS) and the off-center distance of the CM stripe (ODMS). In order to investigate the influence of the two parameters, a numerical simulation model is built based on the optical scheme shown in Fig. 1(a). Primary parameters of the simulation model are listed in Table 1. In the simulation, the 4th to 11th Zernike polynomials in the Noll index are taken as the simulation targets.

3.1. The width of the CM stripe (WMS)

Shown in Fig. 3(a) and (b) [Fig. 3(b) is the zooming display of the area in the red dash line in Fig. 3(a)] is the intensity distribution at the focal plane, including the focal spot and the CM. According to Eq. (1), the 2D-PSD distribution is the quadratic modulus of the far-field self-correlation, and it can be calculated from the near-field profile in practical application. In the self-correlation process, when the CM stripes overlapping with the focal spot, four cross dark lines will appear in the PSD distribution of the output near-field profile, as shown in Fig. 3(c) and (d) [Fig. 3(d) is the zooming display of the area in the red dash line in Fig. 3(c)], which reflects the relative distance between

Table 1
The optical parameters of the simulation model.

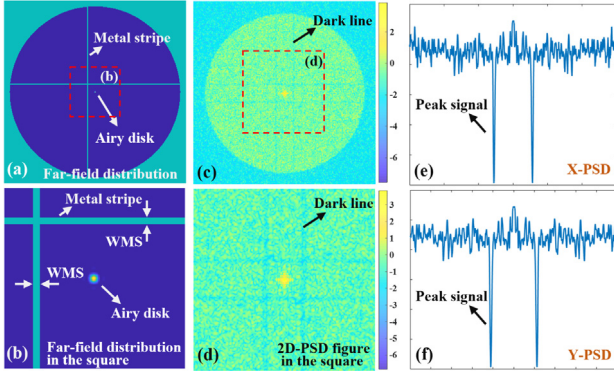| Parameters	Wavelength	Aperture of the incident beam	Focal length of L1	Focal length of L2	Resolution of the CCD	Number of the sub-beams
Value	1.053 μm	360 mm × 360 mm	12 m	12 m	2048 × 2048	16 × 16

Fig. 3. (a) is the intensity distribution at the focal plane, and (b) is the zooming display of the area in the red dash line in (a). (c) is the 2D-PSD of the output near-field profile, and (d) is the zooming display of the area in the red dash line in (c). (e) and (f) are the X-PSD and Y-PSD curves in X-direction and Y-direction respectively.

Fig. 4. X-PSD curves with the WMS setting as (a) 0.3 DL, (b) 0.4 DL, (c) 0.5 DL, (d) 1.0DL and (e) 1.5DL respectively.

Fig. 5. Metal stripes and far-field distribution in the log-coordinate at the focal plane.

the focal spot and the metal stripes. In order to make the dark lines more distinct to be identified, the logarithmic 2D-PSD data in the red dash line area in Fig. 3(c) [i.e. Fig. 3(d)] are directly accumulated along Y-direction and X-direction to be X-PSD [Fig. 3(e)] and Y-PSD [Fig. 3(f)] respectively. Two peaks in the X-PSD and Y-PSD curves represent vertical and transverse dark lines in the 2D-PSD distributions, respectively. In the simulation, according to Eq. (2), the positions of the peaks are used to calculate the wavefront slopes. Based on this principle, the precision of the acquired wavefront slope is determined by the measurement precision of the position.

In general, the sub-beam is approximate to an absolute tilt wave, and its focal spot is an Airy-disk (most energy concentrated within 1-time DL). Here, DL is the diffraction limit of the square sub-beam, defined in Eq. (3).

$$1DL = \frac{2\lambda f}{D_{sub}}. \tag{3}$$

where λ is the wavelength of the incident beam, f the focal length of the input lens [i.e. L1 in Fig. 1(a)], and D_{sub} the size of the sub-beam. In order to clarify the relationship of the WMS and the corresponding Airy-disk radius [Eq. (3)], the WMS will take the DL of the sub-beam as the unit in the following simulation.

Fig. 4 shows the X-PSD curves with the WMS set as 0.3DL, 0.4DL, 0.5DL, 1DL and 1.5DL respectively. When the WMS is set 0.3DL, the peak signals are almost covered by the background noise and very difficult to be recognized [Fig. 4(a)]. When the WMS is set 0.4DL, although emerging from the background noise, the amplitudes of the peak signals are still very small and the profiles are not in regular shape, which might bring calculation errors when achieving the accurate positions of the peak signals [Fig. 4(b)]. When the WMS is set 1.5DL, the peak signal becomes high enough to be identified clearly, but the top part is distorted due to the modulation noises generated with the increasing of the full width at half maximum [Fig. 4(e)], which will influence the calculation precision of the peak position. When the WMSs are set 0.5DL and 1.0DL, the peak signals are both high and clear, while the profiles are sharp with little distortion [Fig. 4(c) and (d)]. Based on the information of Fig. 4(c) and (d), positions of the peak signals could be obtained in high precision. Note that in the Y-PSD [Fig. 3(f)], the WMS has the same influence on the peak signal and will not be discussed here for simplicity's sake. According to the above analysis, the WMS
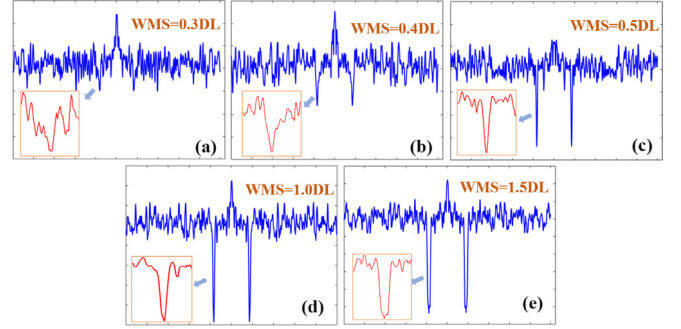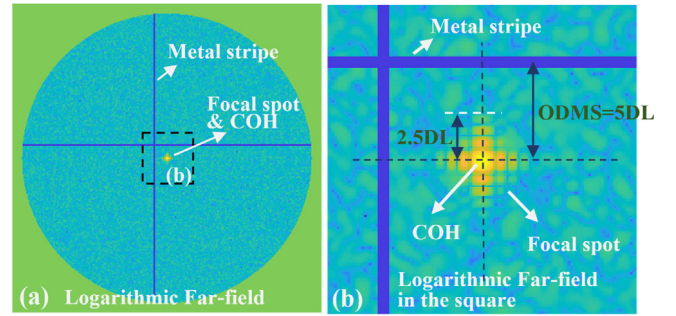
could be designed within the range from 0.5DL to 1DL to acquire high wavefront sensing accuracy and reduce the manufacture difficulty of the slim CM stripes in practical operation.

3.2. Off-center distance of the CM stripe (ODMS)

As described above, the off-center distance of the CM stripe is the distance between the metal stripe and the COH. As shown in Fig. 5(a) and (b) [Fig. 5(b) is the zooming display of the area in the black dash line in Fig. 5(a)], supposing the incident beam is an ideal plane wave, the focal spot will locate right at the COH. Fig. 5 shows the relationship between the CM stripes and the far-field distribution in log-coordinate at the focal plane. Most intensity of the focal spot concentrates within a small area (2.5DL radius circle in general), while other high frequency diffracted components disperse around the focal spot with weak intensity. Based on principle of the NIA wavefront sensing method, in the self-correlation process, when the CM stripes overlapping with the focal spot, cross dark lines will generate in the PSD distribution of the output near-field profile, and the wavefront slopes could be calculated based on the positions of the dark lines. In order to make the dark lines much more distinct, the CM stripes should be set off-center to avoid covering the relatively strong intensity region of the focal spot. Typically, for the 2.5DL radius focal spot, the off-center distance of the CM stripe should at least be set larger than 2.5DL [e.g. 5DL in Fig. 5].

Fig. 6 shows the X-PSD curves with the ODMS set as 10DL, 5DL, 2.5DL and 2DL. When the ODMS is set 10DL or 5DL, both peak signals are strong and sharp enough to be recognized in high precision, as shown in Fig. 6(a) and (b). When the ODMS is set 2.5DL, the

Table 2
Reconstructed residue of 4th to 11th Zernike polynomial.

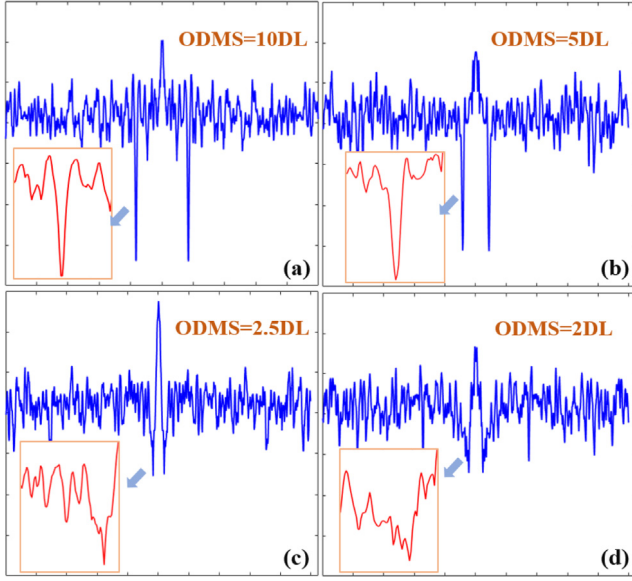| Zernike polynomial	4th	5th	6th	7th	8th	9th	10th	11th
PV (μm)	0.014	0.059	0.060	0.058	0.053	0.079	0.068	0.075
RMS (μm)	0.0019	0.007	0.008	0.004	0.005	0.016	0.01	0.009

Fig. 6. X-PSD curves with the ODMS setting as (a) 10DL, (b) 5DL, (c) 2.5DL and (d) 2DL.

amplitudes of peak signals degrade evidently and the profiles get worse into anomalous shape [Fig. 6(c)], which might affect the calculation precision of the peak signals positions. When the ODMS is set as small as 2DL, the amplitudes of peak signals almost diminish to the level of the background noise and are difficult to be identified [Fig. 6(d)], which may cause serious calculation deviations. According to Fig. 6, in order to obtain the PSD distribution in high signal to noise ratio and increase the calculation precision of the peak signals' positions, the ODMS should be set no less than 5DL. Note that in the Y-PSD [Fig. 3(f)], the ODMS has the same influence on the peak signal and will not be discussed here for simplicity sake.

3.3. The retrieval results in the optimized parameters

According to the analysis above, the influences of the two primary parameters of the CM on the wavefront measurement accuracy are

investigated and the corresponding design principles are also provided. As discussed above, the WMS should set between 0.5DL and 1DL and the ODMS should set at least larger than 5DL in order to achieve high measurement precision.

Fig. 7 shows the calculated wavefront slope, reconstructed wavefront and the residue for the 4th to 11th Zernike polynomials, with the optimized parameters of 0.5DL WMS and 10DL ODMS. The peak-to-valley (PV) and root mean square (RMS) values of the reconstruction residues are listed in Table 2. From Fig. 7 and Table 2, this method performs well in the wavefront measurement, with PV value less than 0.1 μm and RMS value less than 0.01 μm, for the 4th to 11th Zernike modes.

4. Experiment

In order to verify the validity of the NIA wavefront sensing method, an experiment is carried out in a multi-pass amplification high power laser system. As shown in Fig. 8, the multi-pass amplification optical configuration comprises a pre-amplifier, a cavity amplifier, a power amplifier, series of optical lens (L1, L2, L3, L4), a deformable mirror (DM), spatial filters, a liquid crystal on silicon modulator, Farfield-CCD (F-CCD), Nearfield-CCD (N-CCD), a SH wavefront sensor and other components. The laser beam outputs from the pre-amplifier and injects into the main amplifier. Then, the beam (1053 nm, 360 mm × 360 mm aperture) passes cavity amplifier four times and power amplifier three times and extracts enough energy. Finally, the high power laser outputs from the main amplifier and injects into the downstream beamline. The pinhole-array plate (PA, a wheel disk with several groups of pinholes), placed at the focal plane of a spatial filters, is used to filter high spatial frequency components of laser beam and set as the beam reference during alignment process and the fiber head support during wavefront sensing process. In this experiment, the practical CM would be mounted in the hole of PA to modulate the light field. In order to prove the validity of the measuring result of NIA method, the SH sensor locating in the output sensor package is also used to measure the wavefront for comparison.

In the experiment, the wavefront distortion of the pre-amplifier part is taken as the measurement target. In the measurement via the SH wavefront sensing method as shown in Fig. 9(a), a single mode fiber of the laser source is inserted into the first hole of PA1 (PA1-1) to acquire the distortion of the downstream beamline, and the fiber
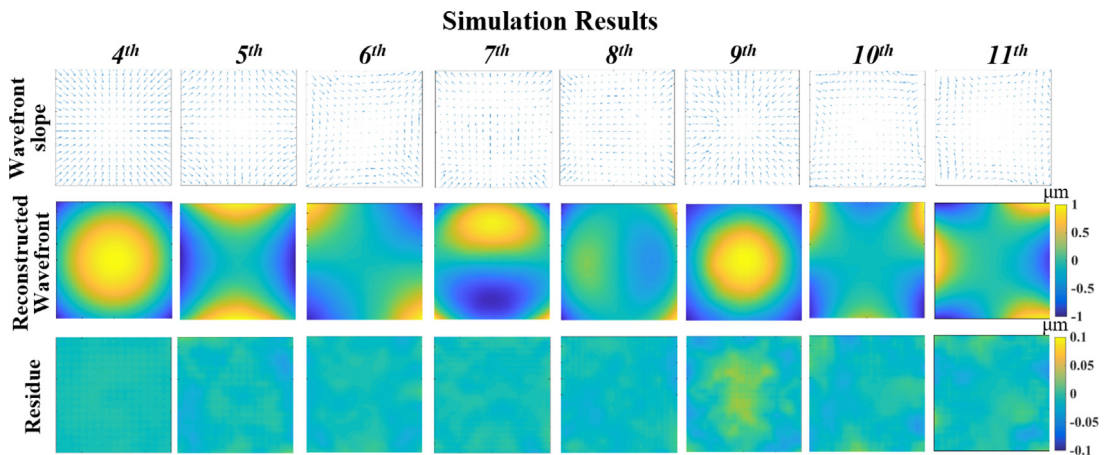

Fig. 7. Reconstructed wavefront and residue. (a) is the wavefront slope, (b) is the reconstructed wavefront and (c) is the residue.
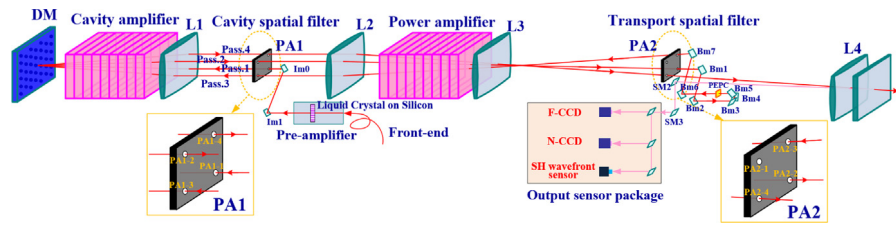
Fig. 8. Multi-pass amplification optical configuration of the high power laser ICF facility. In the beamline, the low energy incident beam is injected into the main amplifier at the focal plane of cavity spatial filter, and amplified three times by cavity amplifier and four times by power amplifier. The far-field intensity, near-field profile and wavefront are measured by Farfield-CCD (F-CCD), Nearfield-CCD (N-CCD) and SH wavefront sensor respectively. PA1 and PA2 are set inside and at the focal plane of cavity spatial filter and transport spatial filter respectively.
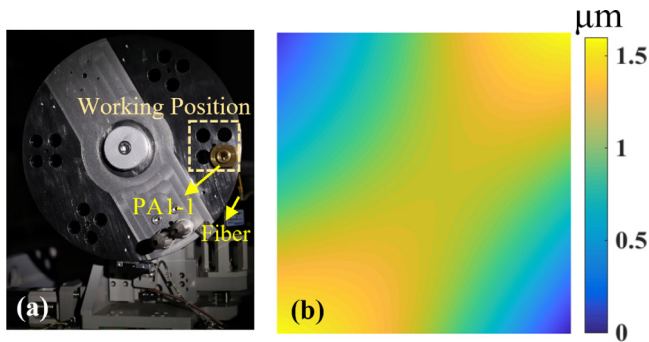

Fig. 9. Photo of the experiment setup and result using the traditional SH wavefront sensing method. (a) is the PA with a single mode fiber inserted in a big hole. (b) is the wavefront measured by the SH wavefront sensing method.
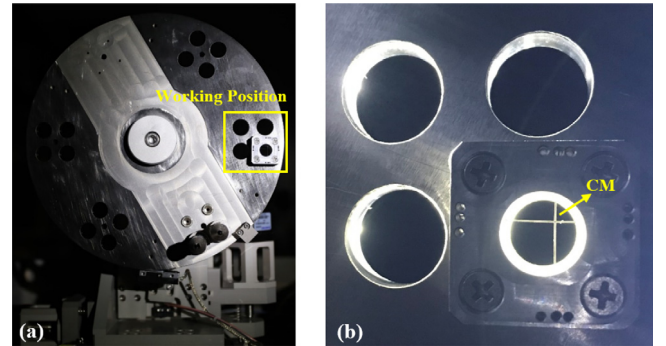

Fig. 10. Photo of the CPMA in the NIA wavefront sensing method experiment. (a) is the cross-mark pinhole-array with a CM mounted on it. (b) is the detailed structure of the CM with two orthogonal metal strips inside.

then is drawn out allowing the incident beam passing through the whole beamline to acquire the distortion of the whole beamline. By subtracting the distortion of the downstream beamline from that of the whole beamline, the target wavefront distortion of the pre-amplifier part is finally measured. Fig. 9(b) shows the measured wavefront via the SH wavefront sensing method, which is taken as the raw wavefront of the beamline to compare with the measurement result of the NIA method. As shown in Fig. 9(b), the measured raw wavefront presents a form of astigmatism aberration with the PV value of 1.59 μm.

According to principle of the NIA wavefront sensing method, in the multi-pass amplification optical configuration, the PA (with CM setting inside), the liquid crystal on silicon modulator in the pre-amplifier (Sony, LCX016AL) and the N-CCD (JAI, BM141-GE, 1392 × 1040 pixels) will be used in the wavefront measurement. Fig. 10(a) shows the PA structure with CM of the NIA wavefront sensing method, consisting of the traditional PA and the CM component which is a metal block with two orthogonal metal stripes set off-center [Fig. 10(b)]. The WMS and ODMS of the manufactured CM are ∼250 μm (i.e. 1.0DL corresponding to the sub-beam in the experiment) and ∼2.5 mm (i.e. 10DL) respectively.

The incident beam [Fig. 11(a)] is divided into 4 × 4 sub-beams by controlling the transmissivity of different segments in the liquid crystal on silicon modulator, and the near-field profile of each sub-beam is acquired by the N-CCD in the output sensor package one by one. Fig. 11(b) shows the first sub-beam near-field profile and the scanning path, which is set from left bottom to right top. Based on the acquired near-field profile of the sub-beam, the logarithmic PSD distribution is calculated accordingly. Fig. 11(c) shows the logarithmic PSD distribution of the first sub-beam near-field profile, in which the four cross dark lines brought by the stripes of the CM are distinct. By accumulating the logarithmic 2D-PSD data [Fig. 11(c)] along X-direction and Y-direction, the X-PSD and Y-PSD curves with peak signals are obtained [white curves in Fig. 11(c)] and the wavefront slope of the sub-beam is calculated according to Eq. (2). By scanning and acquiring the 4 × 4 sub-beams one by one, the 4 × 4 wavefront

slopes distribution can be extracted and displayed in Fig. 11(d). Finally, the wavefront of the laser beam is reconstructed with the PV value of 1.58 μm by using a wavefront reconstruction algorithm. As shown in Fig. 11(e), the measured wavefront presents a form of astigmatism aberration, which is similar to the form of the wavefront measured by the SH wavefront sensing method shown in Fig. 9(b). Fig. 11(f) shows the difference, which mainly occurs in the border and corner region of the sub-beams, between the measured wavefronts by using the traditional SH and NIA wavefront sensing method. As shown in Fig. 11(f), the difference is very small and the PV value is only 0.09 μm.

In the experiment, the WMS is set 1.0DL instead of the optimal value of 0.5DL in consideration of the manufacture cost of the CM. In order to save the measurement time and improve the efficiency, the number of the divided sub-beams is set to be 4 × 4. Based on these parameters, the measurement precision has been closed to the reconstruction precision of the traditional SH wavefront sensing method and met the demand of wavefront measurement in the high power laser facility. In practical application, if higher order wavefront measurement is demanded, the researchers could choose the optimal WMS and larger number for the sub-beams.

5. Conclusion

In conclusion, a novel online NIA wavefront sensing method is presented and experimentally verified in a high power laser system. By introducing the cross-fiducial information at the spectral plane and modulating the high spatial frequency components of the light field, the NIA wavefront sensing method could achieve online wavefront sensing by measuring the near-field profile. Based on the numerical simulation model, the influence of the primary parameters of the cross fiducial on the measurement precision are analyzed and discussed. Simulation results show that the NIA wavefront sensing method has a wide tolerance to the structure parameters and deviations. An experiment is carried out to measure the wavefront of the same beamline by using the traditional SH wavefront sensing method and the presented NIA wavefront sensing
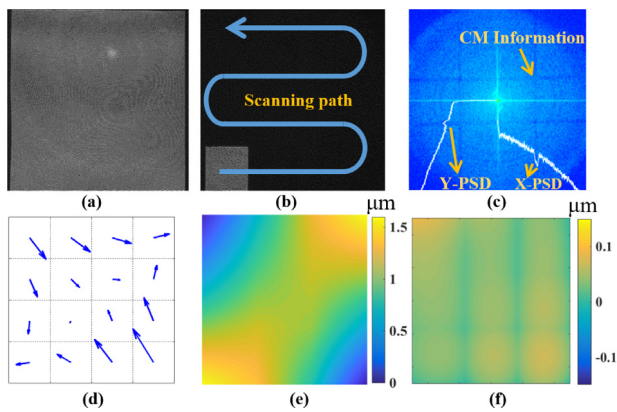
Fig. 11. Wavefront measurement results using the NIA wavefront sensing method. (a) is the nearfield profile of the incident beam. (b) is the near-field profile of each sub-beam along the scanning path. (c) is the logarithmic PSD distribution of the image shown in (b). (d) is the wavefront slope distribution of the sub-beams. (e) is the reconstructed wavefront and (f) is the difference of the reconstructed wavefronts using the traditional SH wavefront sensing method and the NIA wavefront sensing method.

method respectively. In the experiment, the difference between the reconstructed wavefronts by using these two methods is measured to be as small as 0.09 μm (PV value). Experiment results show that the measurement precision of the NIA wavefront sensing method has reached the precision of the traditional SH wavefront sensing method and could meet the demand of wavefront measurement in the high power laser facility.

Declaration of competing interest

The authors declare that they have no known competing financial interests or personal relationships that could have appeared to influence the work reported in this paper.

Funding

References

[1] D.W. Griffin, Phase-shifting shearing interferometer, Opt. Lett. 26 (3) (2001) 140–141.

[2] S. Mousset, C. Rouyer, G. Marre, N. Blanchot, S. Montant, B. Wattellier, Piston measurement by quadriwave lateral shearing interferometry, Opt. Lett. 31 (17) (2006) 2634–2636.

[3] X. Zhou, R. Guo, W. Zhu, D. Zheng, L. Chen, Dynamic wavefront measurement with a pinhole linear polarizer point-diffraction interferometer, Appl. Opt. 56 (29) (2017) 8040–8047.

[4] M.A.A. Neil, M.J. Booth, T. Wilson, New modal wave-front sensor: a theoretical analysis, J. Opt. Soc. Amer. A 17 (6) (2000) 1098–1107.

[5] F. Ghebremichael, G.P. Andersen, K.S. Gurley, Holography-based wavefront sensing, Appl. Opt. 47 (4) (2008) A62–A69.

[6] F.P. Kong, A. Lambert, Improvements to the modal holographic wavefront sensor, Appl. Opt. 55 (13) (2016) 3615–3625.

[7] R.V. Shack, B.C. Platt, Production and use of a lenticular Hartmann screen, J. Opt. Soc. Amer. 61 (1971) 656.

[8] F. Xia, D. Sinefeld, B. Li, C. Xu, Two-photon Shack–Hartmann wavefront sensor, Opt. Lett. 42 (6) (2017) 1141–1144.

[9] R. Kasztelanic, A. Filipkowski, D. Pysz, R. Stepien, A.J. Waddie, M.R. Taghizadeh, R. Buczynski, High resolution Shack-Hartmann sensor based on array of nanostructured GRIN lenses, Opt. Express 25 (3) (2017) 1680–1691.

[10] F. Roddier, Curvature sensing and compensation: a new concept in adaptive optics, Appl. Opt. 27 (7) (1988) 1223–1225.

[11] M.P. Cagigal, P.J. Valle, X–y curvature wavefront sensor, Opt. Lett. 40 (8) (2015) 1655–1658.

[12] F. Díaz-Doutón, J. Pujol, M. Arjona, S.O. Luque, Curvature sensor for ocular wavefront measurement, Opt. Lett. 31 (15) (2006) 2245–2247.

[13] D. Peter, M. Feldt, PYRAMIR: Exploring the on-sky performance of the world's first near-infrared pyramid wavefront sensor, Publ. Astron. Soc. Pac. 122 (887) (2010) 63–70.

[14] J.X. Wang, F.Z. Bai, Y. Ning, L.H. Huang, S.Q. Wang, Comparison between non-modulation four-sided and two-sided pyramid wavefront sensor, Opt. Express 18 (26) (2010) 27534–27549.

[15] H.Y. Wang, C. Liu, S.P. Veetil, X.C. Pan, J.Q. Zhu, Measurement of the complex transmittance of large optical elements with Ptychographical Iterative Engine, Opt. Express 24 (2) (2014) 959–966.

[16] B. Vohnsen, D. Valente, Surface-plasmon-based wavefront sensing, Optica 2 (12) (2015) 1024–1027.

[17] R. Yazdanni, H.R. Fallah, Application of the speckle-based phase retrieval method in reconstructing two unknown interfering wavefronts, Opt. Lett. 41 (17) (2016) 4087–4090.

[18] Y. Nishizaki, M. Valdivia, R. Horisaki, K. Kitaguchi, M. Saito, Jun Tanida, Esteban Vera, Deep learning wavefront sensing, Opt. Express 27 (1) (2019) 240–251.

[19] R.A. Zacharias, N.R. Beer, E.S. Bliss, S.C. Burkhart, S.J. Cohen, S.B. Sutton, R.L. Van Atta, S.E. Winters, J.T. Salmon, M.R. Latta, C.J. Stolz, D.C. Pigg, T.J. Arnold, Alignment and wavefront control systems of the National Ignition Facility, Opt. Eng. 43 (12) (2004) 2873–2884.

[20] C. Grosset-Grange, J.N. Barnier, C. Chappuis, H. Cortey, Design principle and first results obtained on the LMJ deformable mirror prototype, Proc. SPIE 6584 (2007) 658403.

[21] J. Bromage, S.W. Bahk, D. Irwin, J. Kwiatkowski, A. Pruyne, M. Millecchia, M. Moore, J.D. Zuegel, A focal-spot diagnostic for on-shot characterization of high-energy petawatt lasers, Opt. Express 16 (9) (2008) 16561–16572.

[22] D.E. Wang, D.X. Hu, Q. Yuan, Q. Xue, W. Zhou, Y. Yang, X. Zhang, X.W. Deng, Y.C. Wang, J.P. Zhao, W. Deng, X.F. Wei, W.J. Dai, J. Jing, Q.H. Zhu, W.G. Zheng, Wavefront control of main-amplifier system in the SG-III laser facility, Opt. Commun. 394 (2017) 92–97.

[23] Y. Yang, Q. Yuan, D.E. Wang, X. Zhang, W.J. Dai, D.X. Hu, Q. Xue, X.L. Zhang, J.P. Zhao, F. Zeng, S.Z. Wang, W. Zhou, Q.H. Zhu, W.G. Zheng, Object-oriented wavefront correction in an asymmetric amplifying high power laser system, Laser Phy. Lett. 15 (5) (2018) 055001.

[24] S.Z. Wang, Q. Yuan, F. Zeng, X. Zhang, J.P. Zhao, K.H. Li, X.L. Zhang, Q. Xue, Y. Yang, W.J. Dai, W. Zhou, Y.C. Wang, K.X. Zheng, J.Q. Su, D.X. Hu, Q.H. Zhu, Beam alignment based on two-dimensional power spectral density of a near-field image, Opt. Express 25 (22) (2017) 26591–26599.

[25] J. Heebner, M. Borden, P. Miller, S. Hunter, K. Christensen, et al., Programmable beam spatial shaping system for the National Ignition Facility, Proc. SPIE 7916 (2011) 79160H.

[26] M. Barczys, S.W. Bahk, M. Spilatro, D. Coppenbarger, E. Hill, T.H. Hinterman, R.W. Kidder, J. Puth, T. Touris, J.D. Zuegel, Deployment of a spatial light modulator–based beam-shaping system on the OMEGA EP laser, Proc. SPIE 8602 (2013) 86020F.